

Article

Determination of Curie Point Depth Distribution and Heat Flow Regime Characteristics in Eratosthenes Seamount, Eastern Mediterranean Sea

Fayez Harash ^{1,2,*}  and Chao Chen ^{1,3}

¹ State Key Laboratory of Geological Processes and Mineral Resources, School of Geophysics & Geomatics, China University of Geosciences, Wuhan 430074, China

² Geology Department, Faculty of Sciences, Damascus University, Damascus 0100, Syria

³ Hubei Subsurface Multi-Scale Imaging Key Laboratory, School of Geophysics & Geomatics, China University of Geosciences, Wuhan 430074, China

* Correspondence: f.harash@cug.edu.cn

Abstract: The Curie point depth (CPD) has been established to enhance the determination of magnetic sources average bottom depth. In this study, the CPD and heat flow regime of the Eratosthenes Seamount in the Eastern Mediterranean were investigated in order to understand the relationship between them. When CPD and heat flow values are determined together, we can understand the types and processes of geothermal resources formation. CPD and heat flow were obtained by applying the spectral analysis method to magnetic data, which was obtained from the Earth Magnetic Anomaly Grid (EMAG2). The result shows that CPD is approximately 22 km across the Seamount and is approximately 9 km in the northern part of the Eratosthenes Seamount near Cyprus. The heat flow regime manifested from CPD is about 95 mW/m² in the investigated region, where the average thermal conductivity value (*k*) is considered to be 2.5 W/m °C. The heat flow regime is characterized by an increase in the northward part of the Eratosthenes Seamount and decreases towards the south.

Keywords: curie point depth; eratosthenes seamount; heat flow; eastern mediterranean; power spectrum



Citation: Harash, F.; Chen, C. Determination of Curie Point Depth Distribution and Heat Flow Regime Characteristics in Eratosthenes Seamount, Eastern Mediterranean Sea. *Energies* **2022**, *15*, 8634. <https://doi.org/10.3390/en15228634>

Academic Editor: Renato Somma

Received: 9 October 2022

Accepted: 15 November 2022

Published: 17 November 2022

Publisher's Note: MDPI stays neutral with regard to jurisdictional claims in published maps and institutional affiliations.



Copyright: © 2022 by the authors. Licensee MDPI, Basel, Switzerland. This article is an open access article distributed under the terms and conditions of the Creative Commons Attribution (CC BY) license (<https://creativecommons.org/licenses/by/4.0/>).

1. Introduction

The Eratosthenes Seamount is considered one of the most prominent subsurface structures on the Mediterranean seafloor [1]. For several decades, the Seamount has been a subject of interest for many researchers due to its significance in providing information about the oceanography, tectonics as well as geothermal resources of the eastern Mediterranean. It has been established for years that information about Curie point depth (CPD) guides the interpretation and determination of the average bottom depth of magnetic bodies, their sources, and thermal structures [2–14]. Generally, methods utilized for the detection of CPD can be summarized into two main types: geothermal techniques and magnetic techniques. Geothermal techniques rely on the use of geothermal information, such as vertical geothermal ascent and heat flow, based on the conduction and production of the heat of the rocks in the crust [15]. However, there is a constant need to check for errors associated with direct measurement of geothermal factors because of the difficulty of conducting at large depths. Alternatively, magnetic techniques, as exposed by Bhat-tacharyya [16–18], assume that magnetic minerals lose their magnetic properties above Curie temperature values of about 580 °C. Hence, based on this hypothesis, any method that can be used for the estimation of the magnetic bodies' bottom depths in the crust can be extended to detecting CPD. In this investigation, depending on the spectral assessment of magnetic data, the Eratosthenes Seamount was examined in order to assess and approximate the CPD values and heat flow regime. The aim behind this was to understand the relationship between the two data pieces in the eastern Mediterranean region. When

heat flow values and CPD values are assessed with each other, the processes that form geothermal resources can be inferred based on the presence of an unusually hot and thin lithosphere as well as a constant melting degree of the crust, which all play vital roles in forming earth resources [19].

2. Geological and Tectonic Setting

The Eratosthenes Seamount is situated north of the Nile Cone and south of Cyprus and is characterized by a single huge crest nearly 790 m beneath the sea level [20]. As one of the most noticeable bathymetric characteristics in the Mediterranean, the Eratosthenes Seamount is an excellent instance of the start of a collision of a subduction zone with the continental crust, which is joined to the Cyprus continental crust shown in Figure 1. The tectonic evolution of the Eratosthenes Seamount is related to the North African continental margin from the early Mesozoic, according to geophysical and geological studies [21]. The seamount was in a shallow-marine sedimentary setting in the Early Cretaceous, then deactivated to bathyal depths in the Late Cretaceous. Then, in the mid Pliocene–Pleistocene time, the Eratosthenes Seamount was pushed underneath Cyprus due to the collision of the Eurasian Plate and the African Plate [21]. At the time of the Cenozoic, Eratosthenes was moved closer to the Cyprus section of the dynamic edge, and subduction of the oceanic crust (between the African and Eurasian plates) changed to impact [22]. Major structural elements of the Eastern Mediterranean are shown by seismic refraction information [23]. The upper part of the seamount contains deep and shallow water carbonates that belong to the early time of the Cretaceous with tectonic uplift (roughly 1 km). It appears to be the same as the carbonate depositions on the Levant land margin in the east. The neotectonic evolution of the structural features is related to the uplift and emplacement of Troodos Ophiolite in Cyprus [24].

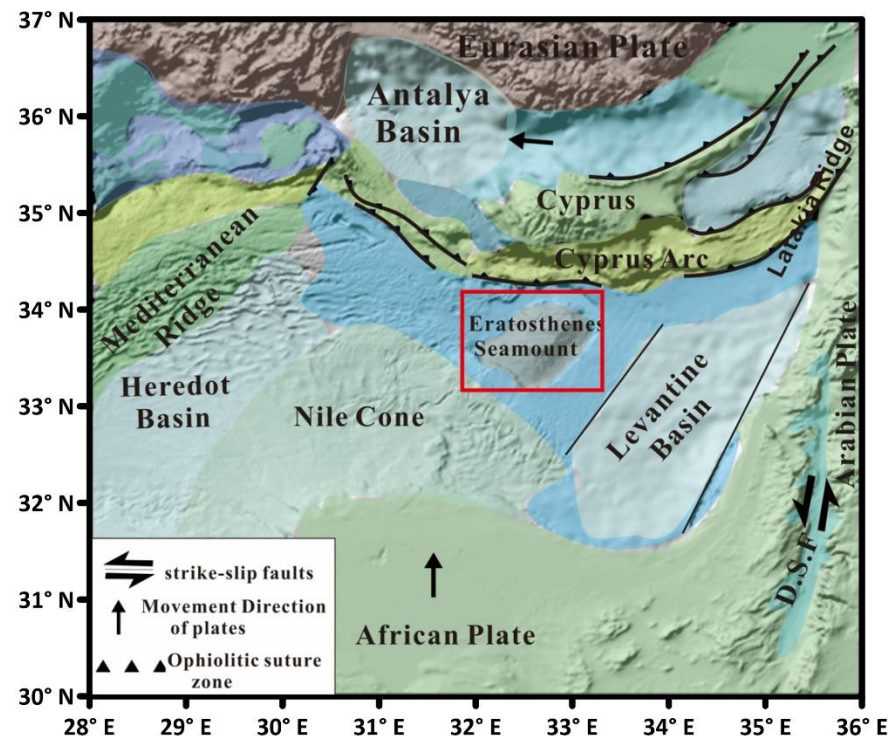


Figure 1. Major tectonic elements of Eastern Mediterranean and the location of the Eratosthenes Seamount, modified from Sage and Letouzey [25].

3. Materials and Methods

Methodology

Many techniques have been introduced and enhanced for determining the bottom depth of the magnetic sources, such as in Spector and Grant [26], who were the first to apply spectrum power method. Then, Okubo [27] and Tanaka [28] proposed the centroid method, which was later modified by Bansal [29] and Nwankwo [30]. However, the spectral method has been established to be one of the most suitable for determining the CPD by checking the spectrum properties of the magnetic anomalies [31–33]. It is the method of choice for this study. It is recommended to be used on a large region because of the difficulty in determining the minor variations of CPD in a small area [33]. This method has been applied in many different regions over the world; Maden [3] used it on the Erciyes Stratovolcano (Central Turkey), Fshar et al. 2016 [34] employed it on the Sabalan Area in NW Iran, and Njeudjang et al. 2020 [12] used it over Adamawa volcanic region (Northern Cameroon). The radial average power spectrum has given good results in detecting the geothermal resources, especially hot springs [35].

The spectral method takes into consideration the estimated values of the bottom depth (Z_b), centroid depth (Z_0), and top depth (Z_t) of magnetic sources by using the Fourier power spectrum logarithm [36].

Blakely [36] described the power spectral density total field anomaly ($\Phi_{\Delta T}$), and it was expanded by Saibi et al. [7] as:

$$\Phi_{\Delta T}(k_x, k_y) = \Phi_M(k_x, k_y) \times F(k_x, k_y), \tag{1}$$

$$F(k_x, k_y) = 4\pi^2 C_m^2 |\Theta_m|^2 |\Theta_f|^2 e^{-2|k|Z_t} \left(1 - e^{-|k|(Z_b - Z_t)}\right)^2, \tag{2}$$

where $M(x,y)$ is magnetization, the term Φ_M represents the magnetization power-density spectrum; the term C_m represents a proportionality constant; the term Θ_m and the term Θ_f represent factors for geomagnetic field and magnetization directions; the term Z_t and the term Z_b represent magnetic sources top depth and bottom depth, respectively. From Equation (2), we can postulate that all expressions are radially symmetric, excluding Θ_m and Θ_f , which are not radially symmetric; however, their radial average is constant, as is the magnetization M for arbitrary sources. We therefore assume that $\Phi_M(k_x, k_y)$ is taken as constant. The radial average of $\Phi_{\Delta T}$ is:

$$\Phi_{\Delta T}(|k|) = A e^{-2|k|Z_t} \left(1 - e^{-|k|(Z_b - Z_t)}\right)^2, \tag{3}$$

where A is a constant and k is the wavenumber. When we have wavelengths less than twice the thickness of the layer, Equation (3) changes to the following formula by applying logarithm:

$$\ln[\Phi_{\Delta T}(|k|)] = \ln[A] - 2Z_t|k| + 2 \ln[1 - e^{-|k|(Z_b - Z_t)}], \tag{4}$$

The exponential term approaches zero for medium and high values of (k), and the logarithm also similarly does. Consequently, Equation (4) changes to be represented by a line and its slope equal to $2Z_t$:

$$\ln[\Phi_{\Delta T}(|k|)] = \ln[A] - 2Z_t|k|, \tag{5}$$

Then Equation (5) will be changed to a new formula with division by 2 as:

$$\ln\left[\Phi_{\Delta T}(|k|)^{1/2}\right] = B - Z_t|k| \tag{6}$$

where the term B is a constant.

Here, by using Equation (6) we calculate the spectral power of the magnetic data in the study area, the radial average, and d , the slope of long wavelengths, in order to obtain Z_t .

We can rewrite Equation (3) as:

$$[\Phi_{\Delta T}(|k|)]^{1/2} = Ae^{-|k|Z_0} \left(e^{-|k|(Z_t-Z_0)} - e^{-|k|(Z_b-Z_0)} \right), \quad (7)$$

where $Z_0 = (Z_b - Z_t)$ is the centroid depth.

We simplified Equation (7) by replacing the final exponential terms with the initial terms in the Taylor series for $n \sim 0$ as:

$$[\Phi_{\Delta T}(|k|)]^{1/2} \sim Ae^{-|k|Z_0} |k|(Z_b - Z_t), \quad (8)$$

$(Z_b - Z_t)$ is defined as the magnetic source thickness. Equation (8) could be rewritten by applying logarithm as:

$$\ln \left\{ \left[\Phi_{\Delta T}(|k|)^{1/2} \right] / |k| \right\} \approx \ln D - |k|Z_0, \quad (9)$$

where the term D is a constant and $[\Phi_{\Delta T}(|k|^{1/2})/|k|]$ is the spectrum of scaled amplitude. Thus, the estimated values of the top depth (Z_t) and centroid depth (Z_0) of magnetic sources would need two spectral plottings utilizing Equations (6) and (9), respectively. Cross plotting wavenumber k with power spectrum $\ln [\Phi_{\Delta T}(|k|)^{1/2}]$ and plotting a straight line will give us magnetic source depth. The values corresponding to the high wavenumber will give us the top of the source and vice-versa and directly compute the magnetic source bottom depth [27,28]. Thus, a Curie point depth estimation of Z_b is computed from Equation (10):

$$Z_b = 2Z_0 - Z_t, \quad (10)$$

The heat flow is calculated by using Fourier's law [37] as expressed in Equation (9). We create a new map to demonstrate heat flow, where estimated values of dz were used, and Curie temperature (dT) is 580 °C in the igneous rocks. According to many authors, most crystalline rocks consist of magnetite minerals having a Curie temperature of around 580 °C [10,27,28,38,39]. The $\frac{dT}{dz}$ value represents the geothermal ascent from the earth's surface to the top depth of magnetic sources and relates to the heat flow in the following equation [27]. The average thermal conductivity value (k) is assumed as 2.5 W/m °C [14,38–40].

$$q = -k \left(\frac{dT}{dz} \right), \quad (11)$$

where the heat-flux is represented by the term q and the coefficient of thermal conductivity is represented by the term k ; the negative sign means that the heat flow follows the lower temperature direction.

The mean value of the crust earth is 2–2.5 W/m °C [41–43], and we assume this value in our study here as it has been used before [14]. The thermal conductivity is affected by pressure and temperature where the heat conductivity decreases with temperature increment [43–45], but the relationship between them is not fixed.

According to Eucken's experimental law [46], the thermal conductivity of a crystalline insulator is directly proportional to its absolute temperature [47]:

$$\frac{1}{k} = \text{const.} \cdot T, \quad (12)$$

Litovsky and Shapiro [48] simplified the mentioned formula above as follows:

$$k_0 = (C + DT)^{-1}, \quad (13)$$

where C and D are constants that vary with materials. For the determination of the thermal

conductivity in the upper-crust, Čermak and Rybach [49] follow this formula:

$$k_0 = \frac{k}{1 + cT}, \quad (14)$$

where k is the thermal conductivity at 0°C under the shallow surface pressure and C is the material constant, the values of which are in the range of $0\text{--}0.003^\circ\text{C}^{-1}$.

The inversion here is to convert the magnetic anomaly to obtain Curie point depths, including the magnetic sources bottom depth, centroid depth, and top depth.

Following the data preparations, the RTP data was exposed to a low-pass filter while using cut-off wave numbers at 0.11 rad/km . That depends on the basis of the wavelength of the spectral data [36].

4. Results

Magnetic data covering the investigated area was taken from the global Earth Magnetic Anomaly Grid (EMAG2) with 2 arc min resolution, a height of 4 km over the geoid [50]. The data was converted from geographic coordinates to Universal Transverse Mercator (UTM) projection coordinates with a spacing of 5 km. Figure 2 shows the magnetic anomaly map of the Eratosthenes Seamount, while Figure 3 represents the reduction of the magnetic data to the pole (RTP) in order to eliminate the deflection resulting from the magnetic field of the Earth [36].

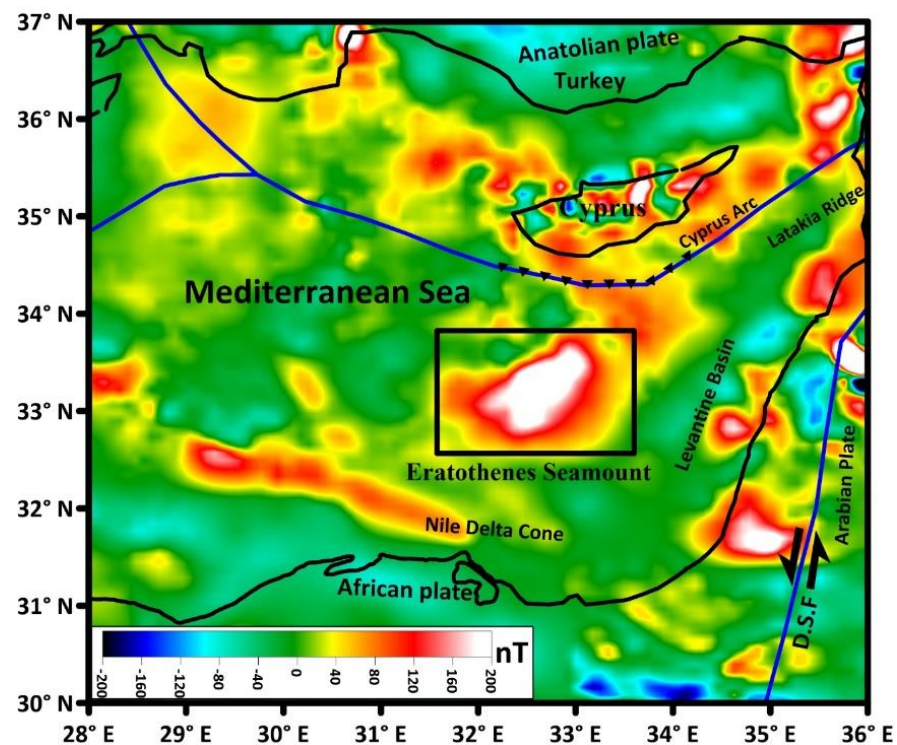


Figure 2. Magnetic anomaly (total field) map of the Eastern Mediterranean (compiled from Maus et al. [50]). The contour intervals are 40 nT.

The Magnetic map of the study area displayed in Figure 2 was processed to obtain the RTP map in Figure 3, which shows that magnetic anomalies are centered on the causative bodies. RTP anomalies range between -200 nT and 200 nT , where the highest magnetic values were noticed in the Eratosthenes Seamount and some parts of Cyprus, while the lowest ones were observed in the Nile delta cone and northern part of the Red Sea.

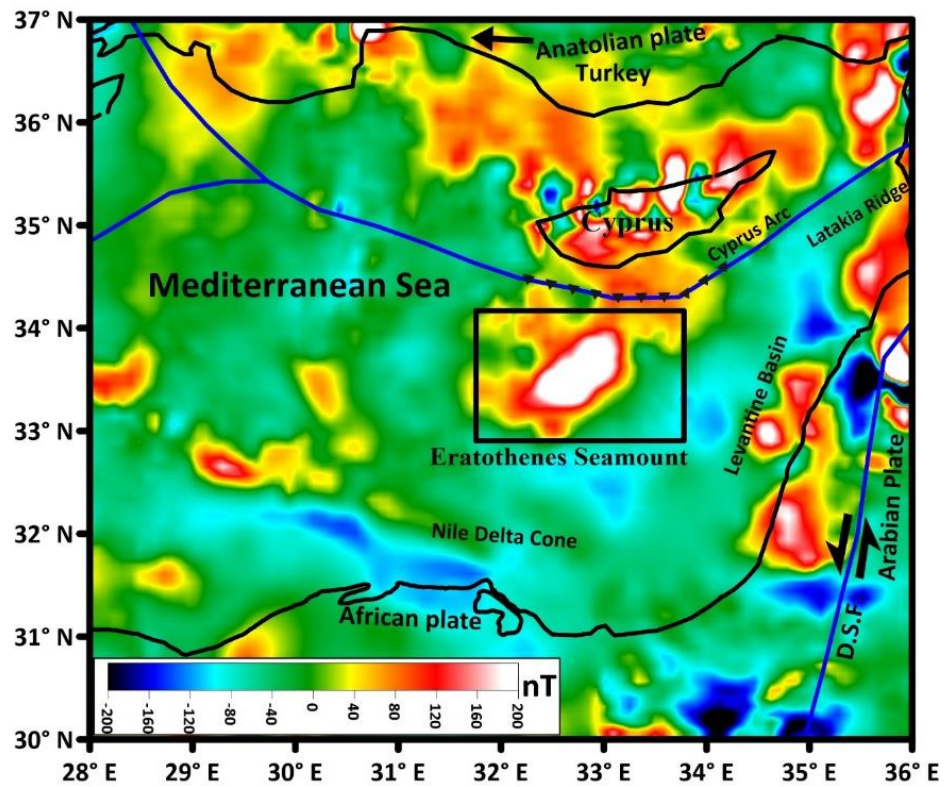


Figure 3. Reduction to pole (RTP) magnetic anomaly map. The contour interval is 40 nT.

By using the power spectrum method of the magnetic anomalies of the study area to determine Z_t and Z_0 , first we obtained the centroid depth (Z_0) of the magnetic source, then calculated the top depth of the magnetic source (Z_t) from the slope of the longest wavelength (Figure 4a,b). Z_0 and Z_t were determined as 9.12 and 2 km, respectively. Applying formula (10) yielded a CPD value of 16.24 km.

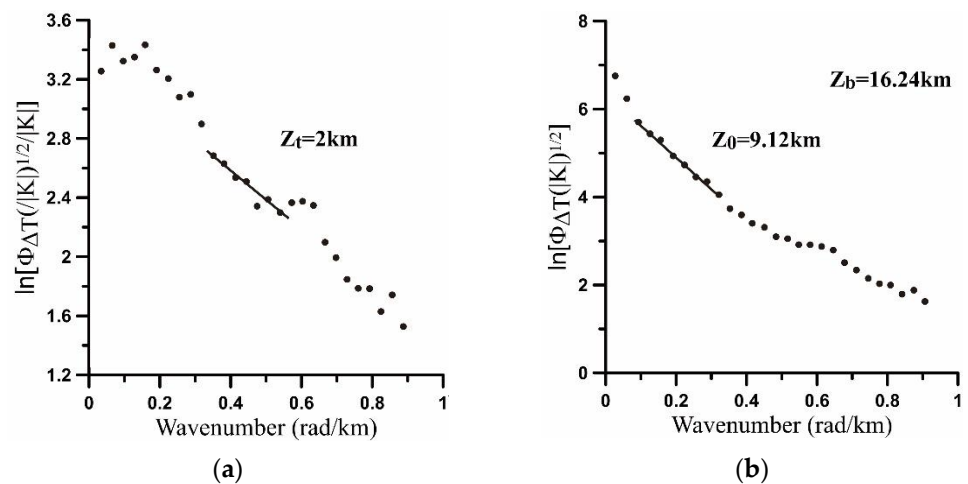


Figure 4. Average power spectrum scheme for CPD estimated in the study area beneath the central part of the Eratosthenes Seamount: (a) top depth in the study area; (b) centroid depth in the study area.

Figure 5 illustrates the CPD map in the Eratosthenes Seamount, where it increases to the south, having a value of around 23 km. CPD has comparatively decreased to 18 km in the north of the Eratosthenes Seamount under Cyprus, and it is also reduced to the east beneath the Levantine basin. From Equation (11), we have computed the heat flow using magnetite’s Curie temperature value $T = 580 \text{ }^\circ\text{C}$ and the average thermal conductivity

value (k) $2.5 \text{ W/m}^\circ\text{C}$. We obtained a heat flow value between 75 and 100 mW/m^2 . The minimum geothermal anomaly has been described as less than 75 mW/m^2 , located at the borders of the Eratosthenes Seamount, and the highest heat flow values are about 100 mW/m^2 , beneath the center of the Eratosthenes Seamount. Heat flow values are more than 100 mW/m^2 at Cyprus and more than 200 mW/m^2 beneath the Levant basin in the east of our study area presented in Figure 6.

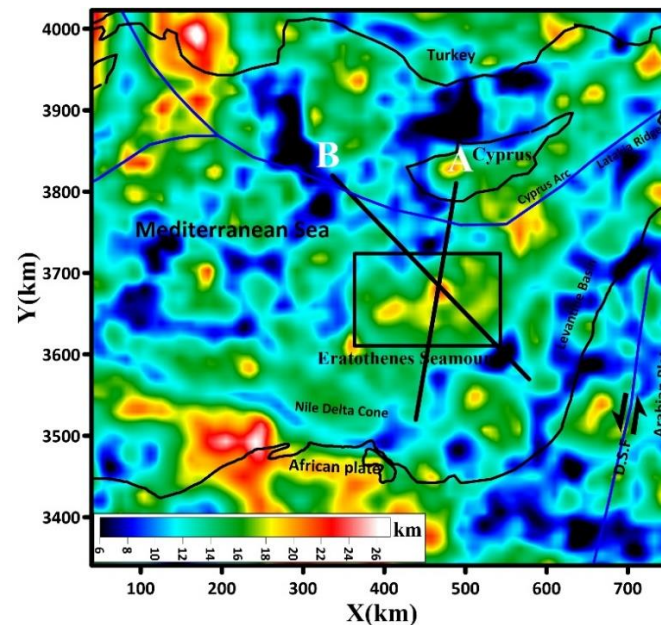


Figure 5. Curie point depth for the Eratosthenes Seamount.

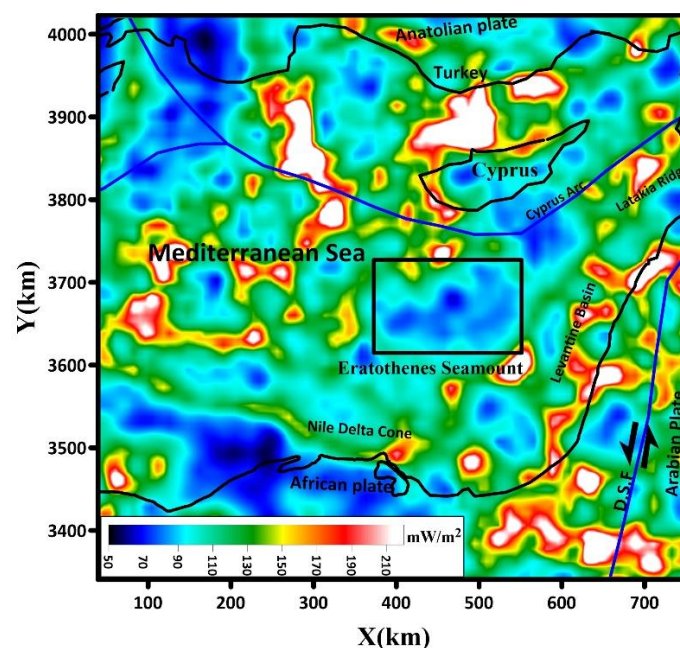


Figure 6. Heat flow map of the Eratosthenes Seamount from Curie point depths.

From the map in Figure 5, two cross-sections were taken along the NE-SW axis, shown in Figure 7a,b, along NW-SE directions. The Curie depth value was estimated to be about 23 km along the A profile under the Eratosthenes Seamount in the south. It begins at 23 km from the North; then it decreases as it approaches the collisional zone between two Eurasian-African plates. There is a slight variation in CPD between the two profiles

where the B Profile Curie depth value begins at approximately 9 km in NW direction, then increases towards SE, where it approaches 14 km in the collisional zone and then increases gradually to reach a peak of 23 km in the Eratosthenes Seamount at the cross point of two profiles A & B. Referring to Figure 7, the Moho depth value decreases from northeast to southwest, approaching a value of 22 km under the Eratosthenes Seamount; the sea bottom beneath the Eratosthenes Seamount is about 1000 m, as shown in (Figure 7a,b).

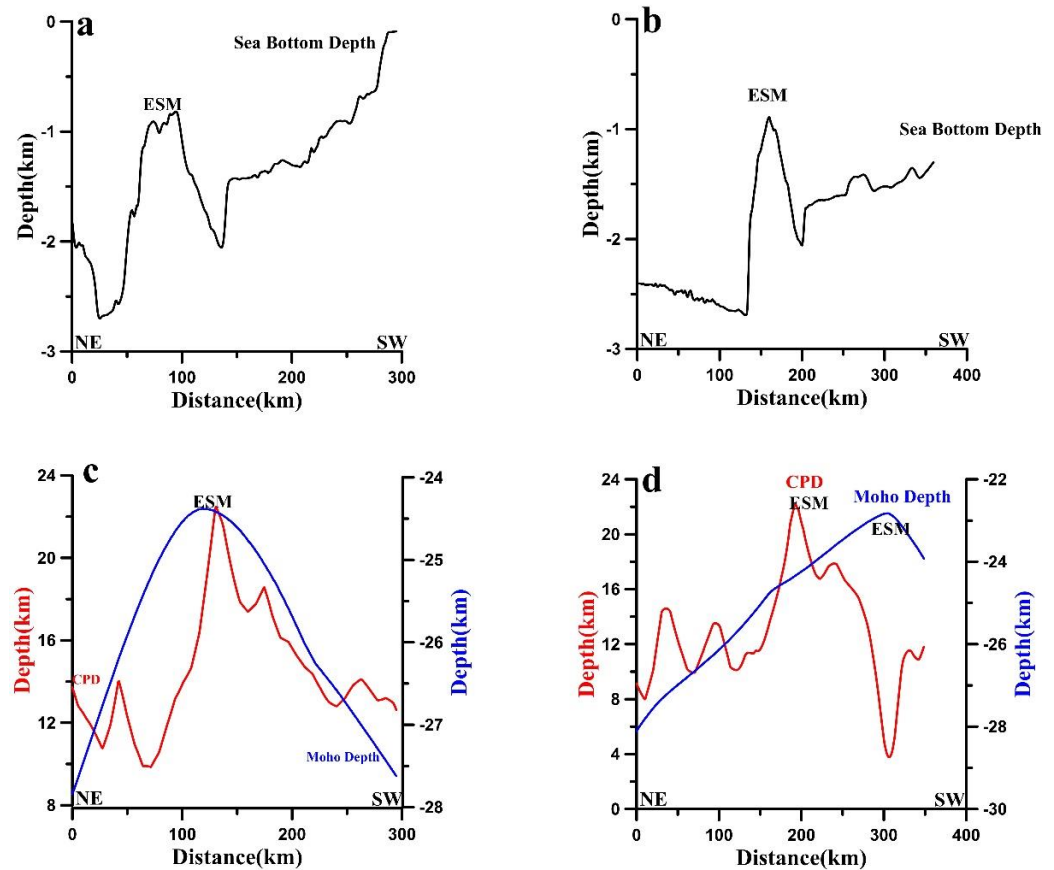


Figure 7. Cross-sections of the CPD map plot along (A) NE-SW and (B) NW-SE directions (profile locations are shown in Figure 5) demonstrating the variation of the Curie point depth, Moho depth and sea bottom depth. (a) the sea bottom depth along profile A, (b) the sea bottom depth along profile B, (c) Moho depth (blue color), CPD (red color) along profile A and (d) Moho depth (blue color), CPD (red color) along profile B.

Such a division of the Eratosthenes Seamount is mainly controlled by its geothermal regime, which plays a significant role in the evolution of the Eastern Mediterranean tectonics including the Troodos ophiolite uplift of Cyprus. This critical role implies an important early collisional phase in the process of plate suturing and mountain building. The high heat flow in this area is ascribed to the higher geothermal potential, so this region is considered a good source for producing geothermal energy, as the shallow Curie depths are frequently associated with active geothermal regions. The tectonic uplift of the Eratosthenes Seamount and the isotherm depression caused by upper-mantle upwelling could be the main geological factors related to such high heat flow factors to generate the heat flow [20,51]. These relatively high values of heat flow are clearly evidenced in Figure 6.

In this study, combining the Curie point depth, obtained by applying the spectrum method of magnetic data, with the calculated heat flow values reveals an inverse relationship between the two, as illustrated in Figures 5 and 6.

5. Discussion

In this study, we computed the CPD depths and heat flow values by applying the power spectrum of EMAG2 data. Our results have shown the negative correlated relation between CPD and heat values, which highlights the presence of major relatively shallow heat sources in the area. This phenomenon in the Eratosthenes Seamount, along with intense faulting and subsidence as a consequence of an early collision of the Eurasian and African plates between the Pliocene and Pleistocene, resulted in the uplifting of southern Cyprus. On the other hand, friction from the collision zone, as well as plutonic intrusions, may be the main controlling factors of such relatively elevated values of heat flow. The upper-mantle upwelling heats the lithosphere underneath the Eratosthenes Seamount and causes the melting that replaces the cold materials in the lithosphere of the Mediterranean Sea. In other words, the mantle convection plays a big role in forming all geological features in the region [52,53]. However, that was caused by an elevated mantle lithosphere beneath the Eratosthenes Seamount as dense block in the lithosphere, which leads to a compressional push-up mechanism for this seamount. The Eratosthenes Seamount is considered a bulky sub-rectangular northward continental part separated from the African plate [54,55], which was raised as a feature in the Eastern Mediterranean Sea beside the Levant basin and Cyprus. It was uplifted as a result of the collision of the Eratosthenes Seamount with Cyprus in the northern direction during the early Miocene [53]. Robertson [53] suggested that the main reason for the Eratosthenes Seamount uplift is associated with the effects of regional tectonic upwarping, which is related to the northern subduction origination of the remnant of Neotethys oceanic crust in the Mediterranean Sea. In the late Pliocene to early Pleistocene the crust thickened over the subduction of the African Plate below the Eurasia.

It, therefore, becomes more evident how the high heat flow values and shallow CPD values have a strong correlation with geothermal and volcanic area crustal thinning. The higher values could be caused by crustal thinning as established by Tanaka [30] and Pamukçu et al. 2014 [19]. The crustal thinning is less than 23 km beneath the Eratosthenes Seamount, as it has a complex structure that varies between the thick upper crust and thin lower crust [56]. During the subduction mechanism between the African–Eurasian Plates, the African plate experiences frictional melting. Then the upper mantle rises toward the lower crust, forming diapirs. As a result, there is a noticeable increase in the heat flow values and a decrease in CPD values in the areas near the mantle diapirs.

The presence of this subduction zone is well established from evidence interpreted from seismic refraction data [52]. As indicated by this confirmation, there is a similarity in the composition of the crust underneath both Cyprus and the Eratosthenes Seamount. Moreover, it can be concluded that structural emplacement of the Troodos ophiolite onto the Eratosthenes Seamount indicates an uncommon case of present-day obduction, in which oceanic crust is thrust above a continental crust [53]. The heat flow map displayed in Figure 6 clarifies the geothermic nature of the study area and gives us a hint that the shallow CPD temperature relies on the morphology and tectonic regime in the Mediterranean Sea.

The magnetized body causing the Eratosthenes magnetic anomaly beneath the seamount is related to magnetite-rich basic volcanics, like those of the Troodos ophiolite, which might be mafic or ultramafic, at a depth of 2–4 km underneath the seafloor [20,22,57,58]. Ben-Avraham et al. 1976 [20] mentioned that the polarized block which causes the Eratosthenes magnetic anomaly may have been pivoted counterclockwise since its formation. Using seismic refraction constraints, it is proposed that the Eratosthenes magnetic anomaly is produced by a typical magnetized high-susceptibility block (2×10^{-3} kg/m³ SI units) with a density of 2750 kg/m³ [22,54]. The magnetic properties of the body caused the Eratosthenes magnetic anomaly, demonstrating that the source material has a high magnetization and presumably basic or ultrabasic material [20]. The magnetic source of the Eratosthenes Seamount is mostly curved in shape, and the magnetic anomaly is mainly seen over seamount related to collision tectonic activity.

Curie depth differs between the two cross-sections; the first one is in the south around 450–650 km Easting and 3650–3750 km Northing. The Eratosthenes Seamount has a CPD

that reaches 22 km in the center, which has been previously determined by Özsöz [13]. Toward the northern parts between 450–650 km, the CPD value is around 18 km beneath southern Cyprus, as shown in Figure 2. Comparing the Curie values in our study area with its borders, the Curie depth varies in the south and southeast beneath Cyprus where Curie depth is different between the south and north of Cyprus from 12 km to 28 km [59]. The CPD value increases following the Moho depth direction. It is considered that the crust could be passive if there is a match between the Moho depth and Curie point depth, while any mismatch that occurs could be an indication of active tectonic regime [59]. Consequently, several properties play an essential role in the change of CPD in both instances. Cross-correlation of Moho depth and CPD depths are shown in Figure 7c,d. We noticed here that the Curie depth is higher than the Moho depth in some parts of the region, which gives an interpretation that the Curie temperature is higher than the temperature in the magnetized lithospheric mantle because of a serpentinization process [60,61].

Thus, the heat flow values are generally higher in the northern parts of the Eratosthenes Seamount and decrease in the southern parts, as shown in Figure 6. Furthermore, the heat flow has the high value of nearly 80 mW/m^2 in the north of the Eratosthenes Seamount under Cyprus and the surrounding areas, whereas it approaches around 100 mW/m^2 under the Eratosthenes Seamount. In addition, this approach has been previously achieved by Özsöz [13]. In correlation with other areas beneath southern Cyprus, the heat flow values are in the range of $50\text{--}70 \text{ mW/m}^2$, using thermal conductivity equal to $2.5 \text{ W/m}^\circ\text{C}$ [59]. It is conceivable to argue that lower magnetic values on the RTP map might be related to the thinner magnetic crust where lower CPD or high heat flow values are found.

6. Conclusions

The Eratosthenes Seamount is one of the most geologically interesting and important sites in the eastern Mediterranean with the potential for substantial geothermal resources. This examination uses the power spectrum method on Reduction to the Pole (RTP) magnetic data to evaluate the values of the heat flow regime and Curie depth. Also, we inverted the magnetic anomaly after reducing it to the pole in order to obtain the magnetic resources bottom depth. The centroid depth and top depth of geothermal resources were computed too. The heat flow map was also demonstrated here by applying the Turcotte and Schubert [50] equation to show the relationship between the heat flow and the Curie depth.

Our results show high values of heat flow and shallow values of Curie point depth which seem to be correlated with thinning of the crust in volcanic regions and geothermal activity.

CPD values were found to be approximately 23 km under the Eratosthenes Seamount, while in Cyprus they have been established to be around 18 km. This indicates that the heat flow has higher values of about 100 mW/m^2 , in the northern part of the Eratosthenes Seamount, where the thinnest crust is located. However, lower values reach 80 mW/m^2 in the southern parts. The CPD and Moho depths are connected with an inverse relationship; as the CPD increases, the Moho depth decreases from NE-SW. If the depth to the bottom of the magnetic layer is higher than the Moho depth, it means that the Curie temperature is higher than the temperature in the magnetized mantle. This is congruent with Wasilewski and Thomas [62], who theorized that the minimum magnetic boundary is associated with the rock composition vertical change, indicating that the Moho depth is considered as the lower magnetic boundary.

Author Contributions: Author Contributions: Conceptualization, F.H. and C.C.; methodology, F.H.; software, F.H.; validation, C.C.; formal analysis, F.H.; investigation, C.C.; resources, C.C.; data curation, F.H.; writing—original draft preparation, F.H. and C.C.; writing—review and editing, F.H. and C.C.; visualization, C.C.; supervision, C.C.; project administration, C.C.; funding acquisition, C.C. All authors have read and agreed to the published version of the manuscript.

Funding: This work was supported by Natural Science Foundation of China (Nos. 42174090 and 41604060), the MOST Special Fund from the State Key Laboratory of Geological Processes and Mineral Resources (MSFGPMR2022-4), China University of Geosciences.

Data Availability Statement: The Magnetic data of the investigated region were acquired from the global Earth Magnetic Anomaly Grid (EMAG2) with 2 arc min resolution a height of 4 km over the geoid (Maus et al., 2009 [50]).

Acknowledgments: We express our deep thanks to Shida Sun, Qing Liang, Jinsong Du and Amin Khalaf for their sincere criticisms and helpful advice throughout this research. Thanks are also due to Jamal Abou-deeb of Damascus University for revising the manuscript.

Conflicts of Interest: The authors declare no conflict of interest.

References

1. Mart, Y.; Robertson, A.H.F. Eratosthenes seamount: An oceanographic yardstick recording the late mesozoic—Tertiary geological history of the eastern Mediterranean. *Proc. Ocean. Drill. Program Sci. Results* **1998**, *160*, 701–708.
2. Dolmaz, M.N.; Hisarlı, Z.M.; Usta, T. Curie Point Depths Based on Spectrum Analysis of Aeromagnetic Data, West Anatolian Extensional Province, Turkey. *Pure Appl. Geophys.* **2005**, *162*, 571–590. [[CrossRef](#)]
3. Maden, N. Curie-point Depth from Spectral Analysis of Magnetic Data in Erciyes Stratovolcano (Central Turkey). *Pure Appl. Geophys.* **2010**, *167*, 349–358. [[CrossRef](#)]
4. Rao, C.R.; Kishore, R.K.; Kumar, V.P.; Babu, B.B. Delineation of intra crustal horizon in Eastern Dharwar Craton—An aeromagnetic evidence. *J. Asian Earth Sci.* **2011**, *40*, 534–541. [[CrossRef](#)]
5. Bansal, A.R.; Anand, S.P.; Rajaram, M.; Rao, V.K.; Dimri, V.P. Depth to the bottom of magnetic sources (DBMS) from aeromagnetic data of Central India using modified centroid method for fractal distribution of sources. *Tectonophysics* **2013**, *603*, 155–161. [[CrossRef](#)]
6. Obande, G.E.; Lawal, K.M.; Ahmed, L.A. Geothermics Spectral analysis of aeromagnetic data for geothermal investigation of Wikki Warm Spring, north-east Nigeria. *Geothermics* **2014**, *50*, 85–90. [[CrossRef](#)]
7. Saibi, H.; Aboud, E.; Gottsmann, J. Curie point depth from spectral analysis of aeromagnetic data for geothermal reconnaissance in Afghanistan. *J. Afr. Earth Sci.* **2015**, *111*, 92–99. [[CrossRef](#)]
8. Bilim, F.; Akay, T.; Aydemir, A.; Kosaroglu, S. Curie point depth, heat-flow and radiogenic heat production deduced from the spectral analysis of the aeromagnetic data for geothermal investigation on the Menderes Massif and the Aegean Region, western. *Geothermics* **2016**, *60*, 44–57. [[CrossRef](#)]
9. Xu, Y.; Hao, T.; Zeyen, H.; Nan, F. Curie point depths in North China Craton based on spectral analysis of magnetic anomalies. *Pure Appl. Geophys.* **2017**, *174*, 339–347. [[CrossRef](#)]
10. Pamuk, E. Investigating edge detection, Curie point depth, and heat flow using EMAG2 magnetic and EGM08 gravity data in the northern part of Eastern Anatolia, Turkey. *Turk. J. Earth Sci.* **2019**, *28*, 805–821.
11. Shirani, S.; Kalateh, A.N.; Noorollahi, Y. Curie point depth estimations for northwest Iran through spectral analysis of aeromagnetic data for geothermal resources exploration. *Nat. Resour. Res.* **2020**, *29*, 2307–2332. [[CrossRef](#)]
12. Njeudjang, K.; Kana, J.D.; Tom, A.; Essi, J.M.A.; Djongyang, N.; Tchinda, R. Curie point depth and heat flow deduced from spectral analysis of magnetic data over Adamawa volcanic region (Northern Cameroon): Geothermal implications. *SN Appl. Sci.* **2020**, *2*, 1330. [[CrossRef](#)]
13. Özsoz, İ. Combined qualitative and quantitative regional interpretation of the thermal results of magnetic data in the Eastern Mediterranean Region. *Turk. J. Earth Sci.* **2021**, *30*, 665–680. [[CrossRef](#)]
14. Özer, Ç.; Öztürk, S.; Pamuk, E. Tectonic and structural characteristics of Erzurum and its surroundings (Eastern Turkey): A detailed comparison between different geophysical parameters. *Turk. J. Earth Sci.* **2022**, *31*, 85–108.
15. Blank, L.; Rioseco, E.M.; Caiazzo, A.; Wilbrandt, U. Modeling, simulation, and optimization of geothermal energy production from hot sedimentary aquifers. *Comput. Geosci.* **2021**, *25*, 67–104. [[CrossRef](#)]
16. Bhattacharyya, B.K. Continuous spectrum of the total-magnetic-field anomaly due to a rectangular prismatic body. *Geophysics* **1966**, *31*, 97.
17. Bhattacharyya, B.K.; Leu, L.K. Analysis of magnetic anomalies over Yellowstone National Park: Mapping of Curie point isothermal surface for geothermal reconnaissance. *J. Geophys. Res.* **1975**, *80*, 4461–4465. [[CrossRef](#)]
18. Mohammed, A.; Adewumi, T.; Kazeem, S.A.; Abdulwaheed, R.; Adetona, A.A.; Usman, A. Assessment of geothermal potentials in some parts of upper Benue Trough northeast Nigeria using aeromagnetic data. *J. Geosci. Engin. Environ. Technol.* **2019**, *4*, 7–15. [[CrossRef](#)]
19. Pamukçu, O.; Akçiğ, Z.; Hisarlı, M.; Tosun, S. Curie Point Depths and Heat Flow of Eastern Anatolia (Turkey). *Energy Sources Part A Recovery Util. Environ. Eff.* **2014**, *36*, 2699–2706. [[CrossRef](#)]
20. Ben-Avraham, Z.; Shoham, Y.; Ginzburg, A. Magnetic Anomalies in the Eastern Mediterranean and the Tectonic Setting of the Eratosthenes Seamount. *Geophys. J. R. Astron. Soc.* **1976**, *45*, 105–123. [[CrossRef](#)]
21. Klimke, J.; Ehrhardt, A. Tectonophysics Impact and implications of the Afro-Eurasian collision south of Cyprus from reflection seismic data. *Tectonophysics* **2014**, *626*, 105–119. [[CrossRef](#)]
22. Rybakov, M.; Voznesensky, V.; Ben-Avraham, Z.; Lazar, M. The Niklas anomaly southwest of Cyprus: New insights from combined gravity and magnetic data. *Isr. J. Earth Sci.* **2008**, *57*, 125–138. [[CrossRef](#)]

23. Ergün, M.; Okay, S.; Sari, C.; Oral, E.Z.; Ash, M.; Hall, J.; Miller, H. Gravity anomalies of the Cyprus Arc and their tectonic implications. *Mar. Geol.* **2005**, *221*, 349–358. [[CrossRef](#)]
24. Robertson, A.H.F.; Kidd, R.B.; Ivanov, M.K.; Limonov, A.F.; Woodside, J.M.; Galindo-Zaldivar, J.; Nieto, L. Probing continental collision in the Mediterranean Sea. *Eos Trans. Am. Geophys. Union* **1994**, *75*, 233–248. [[CrossRef](#)]
25. Sage, L.; Letouzey, J. Convergence of the African and Eurasian plates in the eastern Mediterranean. *Pet. Tecton. Mob. Belts* **1990**, 49–68.
26. Spector, A.; Grant, F.S. Statistical Models For Interpreting Aeromagnetic Data. *Geophysics* **1970**, *35*, 293–302. [[CrossRef](#)]
27. Okubo, Y.; Graf, R.J.; Hansen, R.O.; Ogawa, K.; Tsu, H. Curie point depths of the Island of Kyushu and surrounding areas, Japan. *Geophysics* **1985**, *50*, 481–494. [[CrossRef](#)]
28. Tanaka, A.; Okubo, Y.; Matsubayashi, O. Curie point based on spectrum analysis of the magnetic anomaly data in East and Southeast Asia. *Tectonophysics* **1999**, *306*, 461–470. [[CrossRef](#)]
29. Bansal, A.R.; Gabriel, G.; Dimri, V.P.; Krawczyk, C.M. Estimation of depth to the bottom of magnetic sources by a modified centroid method for fractal distribution of sources: An application to aeromagnetic data in Germany. *Geophysics* **2011**, *76*, L11–L22. [[CrossRef](#)]
30. Nwankwo, L.I. Estimation of depths to the bottom of magnetic sources and ensuing geothermal parameters from aeromagnetic data of Upper Sokoto Basin, Nigeria. *Geothermics* **2015**, *54*, 76–81. [[CrossRef](#)]
31. Shuey, R.T.; Schellinger, D.K.; Tripp, A.C.; Alley, L.B. Curie depth determination from aeromagnetic spectra. *Geophys. J. R. Astron. Soc.* **1977**, *50*, 75–101. [[CrossRef](#)]
32. Blakely, R. Curie temperature isotherm analysis and tectonic implications of aeromagnetic data from Nevada. *J. Geophys. Res.* **1988**, *93*, 11817–11832. [[CrossRef](#)]
33. Hussein, M.; Mickus, K.; Serpa, L.F. Curie Point Depth Estimates from Aeromagnetic Data from Death Valley and Surrounding Regions, California. *Pure Appl. Geophys.* **2013**, *170*, 617–632. [[CrossRef](#)]
34. Fshar, A.A.; Orouzi, G.H.N.; Oradzadeh, A.M.; Iahi, M.A.R.; Orkhial, S.P. Curie Point Depth, Geothermal Gradient and Heat-Flow Estimation and Geothermal Anomaly Exploration from Integrated Analysis of Aeromagnetic and Gravity Data on the Sabalan Area, NW Iran. *Pure Appl. Geophys.* **2016**, *174*, 1133–1152. [[CrossRef](#)]
35. Low, U.; Absar, A.; Duraiswami, R.; Singh, A. Geophysical exploration of Tural-Rajwadi group of hot springs, West Coast Geothermal Province, Maharashtra, India and its implications. *Geothermics* **2020**, *88*, 101874. [[CrossRef](#)]
36. Blakely, R. *Potential Theory in Gravity and Magnetic Applications*; Cambridge University Press: Cambridge, UK, 1995.
37. Lowrie, W.; Fichtner, A. *Fundamentals of Geophysics*, 2nd ed.; Cambridge University Press: Cambridge, UK, 1982.
38. Bektaş, Ö.; Ravat, D.; Büyüksaraç, A.; Bilim, F.; Ateş, A. Regional Geothermal Characterisation of East Anatolia from Aeromagnetic, Heat Flow and Gravity Data. *Pure Appl. Geophys.* **2007**, *164*, 975–998. [[CrossRef](#)]
39. Nwankwo, L.I.; Olasehinde, P.I.; Akoshile, C.O. Heat flow anomalies from the spectral analysis of airborne magnetic data of Nupe Basin, Nigeria. *Asian J. Earth Sci.* **2011**, *4*, 20–28. [[CrossRef](#)]
40. Abraham, E.M.; Lawal, K.M.; Ekwe, A.C.; Alile, O.; Murana, K.A.; Lawal, A.A. Spectral analysis of aeromagnetic data for geothermal energy investigation of Ikogosi Warm Spring—Ekiti State, southwestern Nigeria. *Geotherm. Energy* **2014**, *2*, 6. [[CrossRef](#)]
41. Kappelmeyer, O.; Hänel, R. *Geothermics with Special Reference to Application*; Gebrüder Borntrager: Stuttgart, Germany, 1974.
42. Poelchau, H.S.; Baker, D.R.; Hantschel, T.H.; Horsfield, B.; Wygrala, B. *Basin Simulation and the Design of the Conceptual Basin Model*; Welte, D.H., Horsfield, B., Baker, D.R., Eds.; Springer: Berlin, Germany, 1997; pp. 36–41.
43. Eppelbaum, L.; Kutasov, I.; Pilchin, A. Thermal Properties of Rocks and Density of Fluids. *Appl. Geotherm.* **2014**. [[CrossRef](#)]
44. Lubimova, E.A. Thermal history of the Earth. In *The Earth's Crust and Upper Mantle*; Geophysical Monograph Series; American Geophysical Union: Washington, DC, USA, 1968; Volume 13, pp. 63–77.
45. Clauser, C.; Huenges, E. Thermal conductivity of rocks and minerals. In *Rock Physics and Phase Relations: A Handbook of Physical Constants*; Ahrens, T.J., Ed.; American Geophysical Union: Washington, DC, USA, 1995; Volume 3, pp. 105–126.
46. Eucken, A. Dependence of the thermal conductivity of certain gases on the temperature. *Physikal. Zeitsch.* **1911**, *12*, 1101–1107.
47. Petrunin, G.I.; Popov, V.G. Temperature dependence of lattice thermal conductivity of Earth's mineral substance. *Izv. Russ. Acad. Sci. Phys. Solid Earth* **1995**, *30*, 617–623.
48. Litovsky, E.; Shapiro, M. Gas pressure and temperature dependencies of thermal conductivity of porous ceramic materials: Part 1, refractories and ceramics with porosity below 30%. *J. Am. Ceram. Soc.* **1992**, *75*, 3425–3439. [[CrossRef](#)]
49. Cermak, V.; Rybach, L. Thermal conductivity and specific heat of minerals and rocks. In *Landolt-Bornstein Numerical Data and Functional Relationships in Science and Technology*; Angenheister, G., Ed.; Springer: New York, NY, USA, 1982; pp. 213–256.
50. Maus, S.; Barkhausen, U.; Berkenbosch, H.; Bournas, N.; Brozena, J.; Childers, V.; Dostaler, F.; Fairhead, J.D.; Finn, C.; von Frese, R.R.B.; et al. EMAG2: A 2-arc min resolution Earth Magnetic Anomaly Grid compiled from satellite, airborne, and marine magnetic measurements. *Geochem. Geophys. Geosyst.* **2009**, *10*. [[CrossRef](#)]
51. Erickson, A.J. The Measurement and Interpretation of Heat Flow in the Mediterranean and Black Sea. Ph.D. Thesis, Massachusetts Institute of Technology (MIT), Cambridge, MA, USA, 1970.
52. Welford, J.K.; Hall, J.; Christian, H.; Loudon, K. Crustal seismic velocity structure from Eratosthenes Seamount to Hecataeus Rise across the Cyprus Arc, eastern Mediterranean. *GJI Geodyn. Tecton.* **2015**, *200*, 935–953. [[CrossRef](#)]

53. Robertson, A.H.F. Tectonic significance of the Eratosthenes Seamount: A continental fragment in the process of collision with a subduction zone in the eastern Mediterranean (Ocean Drilling Program Leg 160). *Tectonophysics* **1998**, *298*, 63–82. [[CrossRef](#)]
54. Ben-Avraham, Z.; Ginzburg, A.; Makris, J.; Eppelbaum, L. Crustal structure of the Levant Basin, eastern Mediterranean. *Tectonophysics* **2002**, *346*, 23–43. [[CrossRef](#)]
55. Netzeband, G.L.; Gohl, K.; Hübscher, C.P.; Ben-avraham, Z.; Dehghani, G.A.; Gajewski, D.; Liersch, P. The Levantine Basin—Crustal structure and origin. *Tectonophysics* **2006**, *418*, 167–188. [[CrossRef](#)]
56. Segev, A.; Rybakov, M.; Lyakhovsky, V.; Hofstetter, A. The structure, isostasy and gravity field of the Levant continental margin and the southeast Mediterranean area. *Tectonophysics* **2006**, *425*, 137–157. [[CrossRef](#)]
57. Woodside, J.M.; Williams, S.A. *Geophysical Data Report of the Eastern Mediterranean Sea: RRS Shackleton Cruises 3/72, 5/72 and 1/74D*; Cambridge University: Cambridge, UK, 1977.
58. Selim, E.S.; Abouad, E.; Moustafa, S.R.; Al-Arifi, N.S. Active tectonic trends and crustal modeling of the eastern Mediterranean Sea deduced from geophysical data. *Environ. Earth Sci.* **2016**, *75*. [[CrossRef](#)]
59. Pamuk, E.; Özsöz, İ. Estimation of Curie-Point Depths and Heat Flow from Spectral Analysis of EMAG2 Magnetic Data in Cyprus Island. *Ann. Geophys.* **2022**, *65*, 1036. [[CrossRef](#)]
60. Guimarães, S.N.P.; Ravat, D.; Hamza, V.M. Combined use of the centroid and matched filtering spectral magnetic methods in determining thermomagnetic characteristics of the crust in the structural provinces of Central Brazil. *Tectonophysics* **2014**, *624*, 87–99. [[CrossRef](#)]
61. Oliveira, J.T.C.; Barbosa, J.A.; de Castro, D.L.; de Barros Correia, P.; Magalhães, J.R.G.; Filho, O.J.C.; Buarque, B.V. Precambrian tectonic inheritance control of the NE Brazilian continental margin revealed by Curie point depth estimation. *Ann. Geophys.* **2021**, *64*, 213.
62. Wasilewski, P.J.; Thomas, H.H. The Moho as a magnetic boundary. *Geophys. Res. Lett.* **1979**, *6*, 541–544. [[CrossRef](#)]